Arabian Journal of Chemistry (2020) 13, 4538–4552

King Saud University

Arabian Journal of Chemistry

www.ksu.edu.sa
www.sciencedirect.com

ORIGINAL ARTICLE

Fabrication of dual Z-scheme photocatalyst *via* coupling of BiOBr/Ag/AgCl heterojunction with P and S co-doped g-C_3N_4 for efficient phenol degradation

Pankaj Raizada [a,b,*], **Prachi Thakur** [a], **Anita Sudhaik** [a], **Pardeep Singh** [a,b], **Vijay Kumar Thakur** [c], **Ahmad Hosseini-Bandegharaei** [d]

[a] *School of Chemistry, Faculty of Basic Sciences, Shoolini University, Solan, HP 173229, India*
[b] *Himalayan Centre for Excellence in Nanotechnology, Shoolini University, Solan, HP 173229, India*
[c] *Enhanced Composites and Structures Center, School of Aerospace, Transport and Manufacturing, Carnfield University, Bedfordshire MK43 0AL, UK*
[d] *Department of Engineering, Kashmar Branch, Islamic Azad University, P.O. Box 161, Kashmar, Iran*

Received 14 August 2019; accepted 3 October 2019
Available online 15 October 2019

KEYWORDS

BiOBr;
Ag/AgCl;
P and S co-doped g-C_3N_4;
Dual Z-scheme approach;
Enhanced photocatalysis;
Phenol degradation

Abstract Advances in noble metal mediated Z-scheme photocatalytic system have ushered in a climax on environmental remediation. Herein, graphitic carbon nitride (GCN) and phosphorus sulphur co-doped graphitic carbon nitride (PSCN) were synthesized via calcination process. GCN, PSCN and Z-scheme visible light driven (VLD) ternary BiOBr/PSCN/Ag/AgCl nanophotocatalyst were characterized by X-ray diffraction pattern (XRD), Fourier transform infrared (FTIR), X-ray photoelectron spectroscopy (XPS), scanning electron microscopy (SEM), transmission electron microscopy (TEM) and UV–visible diffuse reflectance spectra (UV–vis DRS). BiOBr/PSCN/Ag/AgCl nanocomposite exhibited superior visible light driven photocatalytic ability as compared to pristine PSCN, AgCl and BiOBr towards degradation of phenol. The results explicated promising photocatalytic activity along with space separation of photocarriers caused *via* formation of BiOBr/PSCN/Ag/AgCl Z-scheme heterojunction. The visible light absorption efficacy of BiOBr/PSCN/Ag/AgCl photocatalyst was confirmed by photoluminescence (PL) spectra. Finally, recycling experiments were explored for the mechanistic detailing of phenol photodegradation employing BiOBr/PSCN/Ag/AgCl photocatalyst. After seven successive cycles photodegradation efficacy of photocatalyst was reduced to 90% from 98%. Proposed mechanism of BiOBr/PSCN/Ag/AgCl

* Corresponding author at: School of Chemistry, Faculty of Basic Sciences, Shoolini University, Solan, HP 173229, India.
E-mail address: pankajchem1@gmail.com (P. Raizada).
Peer review under responsibility of King Saud University.

Production and hosting by Elsevier

https://doi.org/10.1016/j.arabjc.2019.10.001

nanophotocatalyst for degradation of phenol was discussed. $OH^{\cdot}$ and $O_2^{\cdot-}$ radicals were main reactive species responsible for photocatalytic phenol degradation.

1. Introduction

Interminable industrialization and economic development lead to serious deficits of water sources. The diminution of energy sources is posing threat to human and environment. However, traditional techniques of water purification such as coagulation, flocculation, precipitation and filtration were employed but these methods are associated with many pitfalls. Therefore, challenge is to develop a nanomaterial engineered as well as sustainable solar light driven heterojunction for waste water purification and environmental recovery. (Sudhaik et al., 2018a; Raizada et al., 2016). Advanced oxidation technologies (AOT) have developed as effective method for water remediation. In 1972, Honda and Fujishima introduced heterogeneous semiconductor photocatalysis with TiO_2 (Priya et al., 2016b; Zhang et al., 2018). Photocatalysis involves strong oxidants holes (h^+) in valence band (VB) and reductants electrons (e^-) in conduction band (CB). Under visible light illumination, electrons in VB get excited to vacant CB forming electron hole pairs (EHP) (Sudhaik et al., 2018b; Banerjee et al., 2015). Reactive oxidation species (ROS) are the result of reaction among holes (h^+) in VB with hydroxide ions (OH^-) or water (H_2O) molecules to form oxidizing hydroxyl radical ($OH^{\cdot}$). Whereas, e^- in VB reduces oxygen (O_2) and forms superoxide radical ($O_2^{\cdot-}$) (Raizada et al., 2019b). ROS species (e^-, h^+, $OH^{\cdot}$, $O_2^{\cdot-}$) released during photocatalysis process significantly participates in photodegradation of organic pollutants into carbon dioxide, water, and inorganic ions. The prerequisite criteria for an efficient photocatalyst includes appropriate band gap and optimized charge carrier separation under solar light illumination (Sudhaik et al., 2018a). Therefore, construction of visible light driven photocatalyst with extended visible light response, improved surface area and supressed charge carrier recombination for photodegradation of organic/inorganic pollutants is still an important challenge.

In search of a robust and cost-effective semiconductor to counter water energy demands, polymeric GCN has gained tremendous attention. It is a n-type metal free semiconducting material, owing tunable band gap (Eg = 2.7 eV) with VB and CB positioned at −1.09 and +1.56 eV respectively (Hu et al., 2019). GCN has attracted much consideration due to its non-toxic nature, greater abundance, good chemical as well as thermal stability with an alluring electronic structure (Xiao et al., 2019b). GCN being a stable visible light driven photocatalysts has become a hot-spot for large scale water purification applications (Zhao et al., 2015). But its photocatalytic performance is restricted due to high recombination rate of photocharge carriers, small surface area and lower absorption of visible light (Sudhaik et al., 2018a). For advancement in photocatalytic performance in solar region numerous approaches i.e. designing porous structure, co-doping (Hasija et al., 2019; Jiang et al., 2008), coupling with another semiconductor (Zhang et al., 2009) have been developed to refine the properties of photocatalyst. Integration of non-metal dopants such as phosphorus (P) and sulphur (S) onto the surface of GCN increased surface area, reduces band gap, thereby providing more reactive sites for enhanced absorption of visible light (Raizada et al., 2020). To date, some investigations have revealed that, in contrast with pristine GCN, S-doped GCN or P-doped GCN flaunts superior visible light activity. Addition of P atom alters the electronic properties, boosts spatial charge separation of photogenerated EHP, expanding surface area thereby enhancing photocatalytic performance. Further, S atom attaches onto N-sites of GCN lattice. From previous reports, it can be concluded that S atom is non-uniformly dispersed leading to shift in fermi level to CB thereby narrowing band gap. Consequently, effective charge separation is attained and photocatalytic efficacy of synthesized co-doped photocatalyst is improved (Hasija et al., 2019). Jiang and co-workers fabricated P and S co-doped GCN (PSCN) as an effective photocatalyst for photodegradation of tetracycline and methyl orange under visible light (Jiang et al., 2017). Chai *et al.* synthesized P doped GCN *via* co-polycondensation method for Rhodamine B degradation (Chai et al., 2017).

Lately, bismuth oxyhalide (BiOX) (X = Cl, Br and I) have received more consideration as efficacious visible light driven photocatalysts (Natarajan et al., 2016; Xiao et al., 2019a; Li et al., 2017). Among these, bismuth oxybromide (BiOBr) is a p-type semiconductor with an indirect band-gap (Eg = 2.91 eV) having matlockite tetragonal assembly. BiOBr being bismuth-based semiconducting material is able to reduce the recombination rate of photoinduced charge carriers (Singh et al., 2018). Huang and co-workers discussed the photocatalytic ability of iodine modified BiOBr photocatalyst, which was greater than that of P25-TiO_2 nanoparticles under visible light illumination (Wang et al., 2008). Wang *et al.* prepared microspherical BiOBr *via* ethylene glycol-assisted solvothermal process (Yanhui et al., 2016). As a result of rapid recombination rate of photoinduced EHP, the photocatalytic performance of BiOBr is not so efficacious. Fabrication of BiOBr hybrids, coupling with another n-type semiconducting materials of suitable energy to form heterojunction have emerged as influential photocatalyst.

Amongst plasmonic photocatalyst, Ag/AgX (X = Cl, Br, I) composites have been employed as new and promising photosensitive semiconductor material for extending visible light absorption (Tang et al., 2011; Guo et al., 2012; Chen et al., 2017). Among these silver halides, silver chloride (AgCl) is a wide band gap semiconductor with indirect band gap of 3.25 eV, possessing VB and CB potentials at +3.16 eV and −0.09 eV respectively, and exhibits some interesting properties (Ye et al., 2014). Upon solar light irradiation AgCl simultaneously absorbs a photon and releases an electron (e^-) and a hole (h^+). The photoinduced electron reacts with interstitial Ag^+ to form metallic Ag^o on the surface of AgCl. Thus, increases the separation of photoinduced electrons and holes exhibiting surface plasmon resonance (SPR) effect (Zhou et al., 2014).

Herein, this work we have successfully fabricated Z-scheme BiOBr/PSCN/Ag/AgCl nanocomposites with the aim of providing substantially upgraded photocatalytic ability under solar light. Incorporation of P and S co-dopants on GCN sheet reduces the band gap, enhances the spatial charge separation thus increasing photocatalytic ability. BiOBr have attracted research interests due to its unique optical, magnetic and electrical properties, stable and absorbs visible light therefore improving photocatalytic efficiency. AgCl a plasmonic photocatalyst behaves as a photosensitive semiconductor with high absorption of solar light and exhibits excellent photodecolouration of organic pollutants due to SPR effect of metallic Ag. Presently, Z-scheme photocatalytic system have gained immense interests due to its stronger redox capability (Wang et al., 2018; Wang et al., 2019). Phenols are considered as poisonous and refractory contaminants and are partially soluble in water. The photocatalytic activity of synthesized nanocomposite was evaluated for photodegradation of phenol. As-prepared nanoheterojunction possesses engineered textural surface, enhanced optical and electronic properties and tailored band gap for the effective degradation of phenol noxious contaminant under natural light.

2. Experimental

2.1. Synthesis of phosphorus sulphur co-doped graphitic carbon nitride (PSCN)

Analytical grade chemicals were employed for synthesis and used as such. Reagents thiourea [CH_4N_2S], ammonium hydrogen phosphate [$(NH_4)_2HPO_4$], bismuth nitrate [$Bi(NO_3)_3 \cdot 5H_2O$], acetic acid [CH_3COOH], potassium bromide [KBr], sodium chloride [NaCl] and silver nitrate [$AgNO_3$] were procured from Sigma Aldrich (India). Deionized water was used for preparation of samples. Briefly P and S co-doped graphitic carbon nitride (PSCN) was prepared by dissolving 3 g of thiourea in 30 mL distilled water and solution was magnetically stirred for 30 min. To this reaction mixture, 0.6 g of $(NH_4)_2HPO_4$ was added and ultrasonicated for next 10 min. The prepared solution was further heated for 20 min to eliminate water and obtained product was dried in hot air oven at 100 °C for 20 min. The obtained precipitates were cooled and annealed at 520 °C for 2 h at a heating rate of 5 °C/min (Digital Muffle Furnace, Model: RSMF-10). Resulting light-yellow coloured product was labelled as PSCN (Raizada et al., 2020).

2.2. Synthesis of bismuth oxybromide (BiOBr) nanocomposite

For synthesis of Bismuth oxybromide (BiOBr) photocatalyst, 1 g Bi $(NO_3)_3 \cdot 5H_2O$ was added to 3 mL of acetic acid in one beaker and in another beaker 0.24 g of KBr was dissolved in 30 mL distilled water. Both solutions were mixed followed by magnetic stirring for 20 min at room temperature. The obtained solution was sonicated for 5 min and kept undisturbed until precipitates settle down. After this mother liquor was washed with distilled water and decant off 2–3 times. Collected precipitates were dried at 100 °C overnight to obtain the solid product. The as-prepared white precipitates were labelled as bismuth oxybromide (Jiang et al., 2010; Singh et al., 2018).

2.3. Synthesis of BiOBr/PSCN/Ag/AgCl nanocomposite

Typically, 0.04 g of NaCl, 0.06 g of $AgNO_3$ were taken in 50 mL and 20 mL of distilled water, respectively and magnetically stirred for 20 min separately followed by ultrasonication for 5 min. Both the solutions were mixed, magnetically stirred and then ultrasonicated for 10 min. In another beaker 1 g BiOBr was dissolved in 100 mL distilled water and magnetically stirred for 15 min. The above obtained reaction mixture was then added dropwise in the BiOBr solution with continuous stirring followed by 30 min ultrasonication. The obtained product was collected, washed with deionised water and kept in hot air oven at 65 °C for 2 h. The as-synthesized precipitates were labelled as binary BiOBr/Ag/AgCl nanocomposite. Now 1 g of PSCN and 0.5 g of binary composite was dissolved in 50 mL and 20 mL of distilled water, respectively and magnetically stirred for 15 min proceeded by ultrasonication for 5 min. Both the solutions were mixed with continuous vigorous stirring and left undisturbed for settling of precipitates. Resultant precipitates were decanted, centrifuged, washed 2–3 times with deionized water/ethanol and dried in hot air oven at 65 °C for 2 h. The synthesized nanocomposite was labelled as ternary BiOBr/PSCN/Ag/AgCl photocatalyst (Fig. 1).

2.4. Characterization techniques

X-ray diffraction (XRD) data was collected *via* Panalytical X'Pert Prodiffractrometer using CuK-α-1 (45 kV/100 mA). Scanning electron microscopy (SEM) analysis were performed *via* model Nava Nano SEM-45 (USA) scheme. Under vacuum environments transmission electron microscopy (TEM) study was attained by model FP/5022-Tecnai G2 S-TWIN(USA) on a randomly selected area functioning at a voltage of 200 kV. KBr pellets were used for the investigation of Fourier-Transform Infrared (FTIR) spectra, obtained using Perkin-Elmer Spectrometer (Spectrum RX-l). The ultraviolet visible (UV–Vis) diffuse reflectance spectra (DRS) was estimated using a diffuse reflectance spectrometer (UV 3600, Shimadzu) in the range 400 to 800 nm. The photoluminescence (PL) spectra of BiOBr/PSCN/Ag/AgCl samples were measured at room temperature on FLS-920 (Edinburgh Instrument).

2.5. Evaluation of photocatalytic activity of BiOBr/PSCN/Ag/AgCl nanocomposite

The photocatalytic ability of fabricated BiOBr/PSCN/Ag/AgCl nanocomposite was investigated for phenol degradation. The slurry type batch reactor was utilized for photocatalytic experimentation owning doubled walled pyrex cylinder with dimensions 7.5 cm × 6 cm (Pare et al., 2009; Pare et al., 2008). 35 W LED lamp was used as a light source to irradiate the reactor. Closed reflux method was employed to determine the chemical oxygen demand (APHA, 1985). Titrating sample with NaOH by means of phenolphthalein as an indicator can be used to measure the dissolved CO_2 (Maiti, 2001). The removal efficacy of the sample was estimated using Eq. (1):

$$\%\ removal = \frac{C_0 - C_t}{C_0} \quad (1)$$

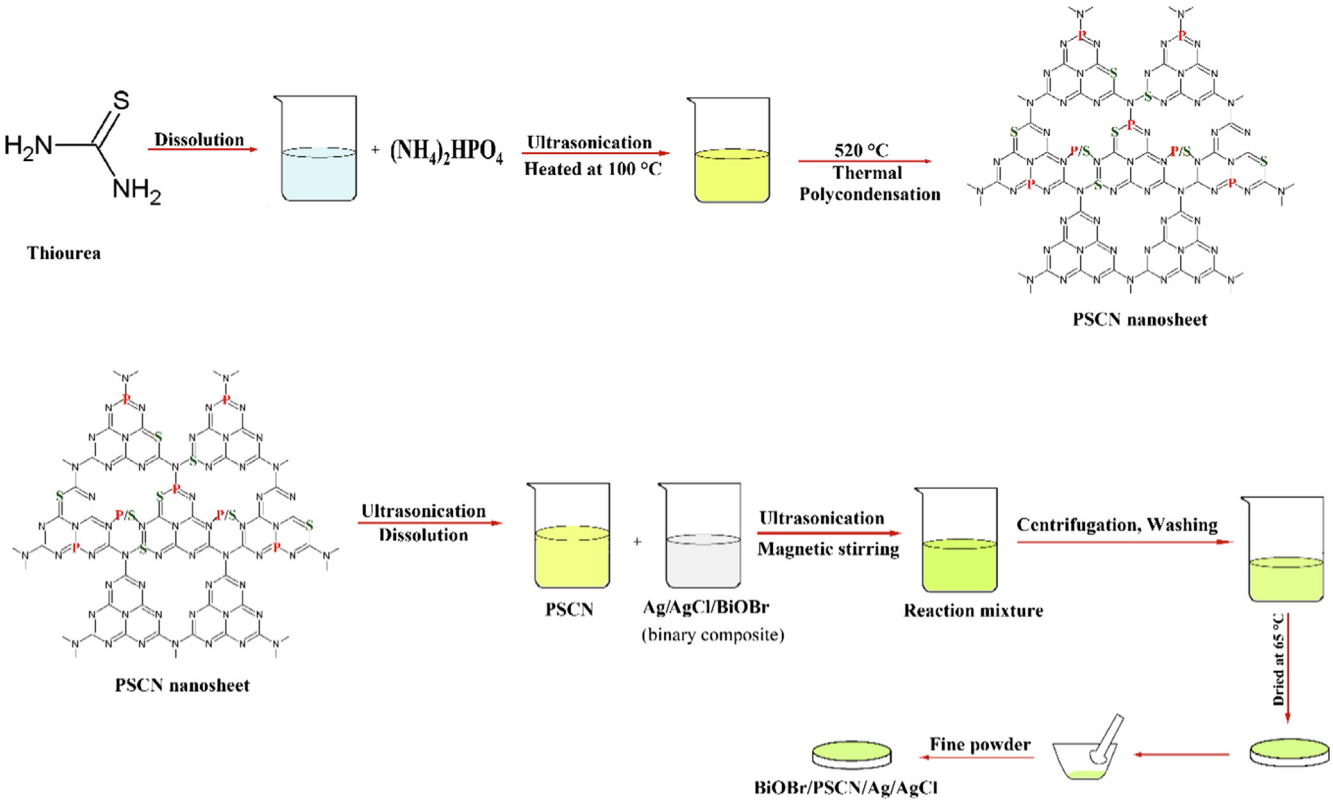

Fig. 1 Schematic illustration for the construction of BiOBr/PSCN/Ag/AgCl heterojunction.

where C_0 represents initial concentration of sample/COD and C_t is instantaneous concentration of sample/COD of phenolic compounds. The device used to calculate the intensity of light was digital lux-meter. All photocatalytic experimentations were accomplished in triplicate with errors under 5% and typical values were stated.

3. Results and discussion

3.1. Characterization of BiOBr/PSCN/Ag/AgCl photocatalyst

3.1.1. XRD and FTIR analysis of BiOBr/PSCN/Ag/AgCl photocatalyst

The crystal structure and phase of as-prepared BiOBr/PSCN/Ag/AgCl photocatalyst was evaluated using XRD technique (Fig. 2). As per reports, characteristic peak of bare GCN was observed around 27.7° which was indexed to {0 0 2} diffraction plane, assigned to interlayer stacking of aromatic rings in GCN (Zhou et al., 2015). XRD patterns of PSCN depicted that P and S co-doping has no observable effect on the morphology of GCN thus, no typical peak was observed which verified incorporation of P, S co-dopants and maintained original structure of GCN (Jiang et al., 2017). The peaks observed around 32.1°, 46.3° and 57.6° were well ascribed to {2 0 0}, {2 2 0} and {2 2 2} diffraction planes of AgCl crystal (JCPDS NO. 31-1238), respectively (Jiao et al., 2019; Zhang et al., 2017). While the diffraction peaks of BiOBr were recorded at 2θ = 25.3° {0 1 1}, 31.6° {0 1 2}, 32.3° {1 1 0}, 43.7° {0 0 4}, 44.6° {0 2 0}, 52.6° {2 1 1}, 54.8° {2 1 4} and 57.2°

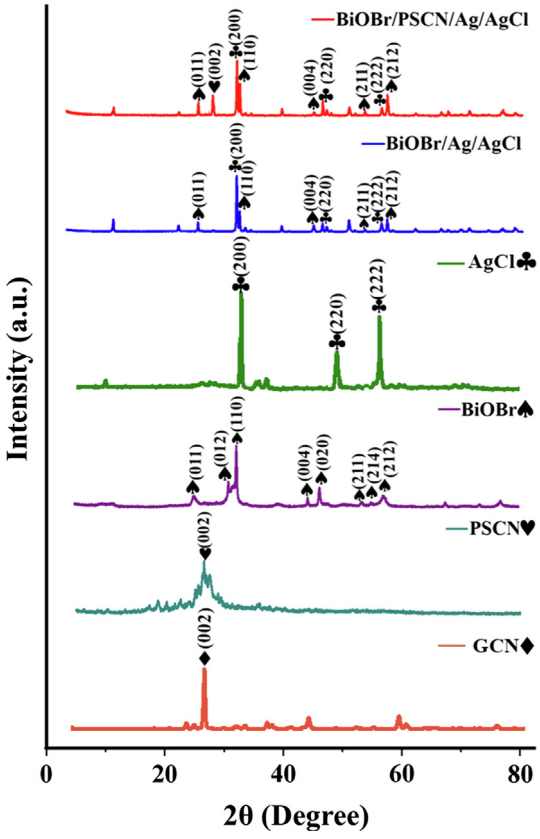

Fig. 2 XRD pattern of PSCN, BiOBr, Ag/AgCl and BiOBr/PSCN/Ag/AgCl.

{2 1 2}, respectively (JCPDS NO. 73-2061) (Singh et al., 2018; Xia et al. 2014).

Moreover, FTIR spectra (Fig. S1) explored structural evidence of fabricated BiOBr/PSCN/Ag/AgCl nanocomposites in the range of 400–4000 cm^{-1}. The band at 805 cm^{-1} signified vibration characteristic of triazine units of PSCN (Raizada et al., 2019a). The absorption peaks ranging between 1200 and 1700 cm^{-1} centered at 1382, 1495 and 1638 cm^{-1} were ascribed to typical —CN stretching existing in PSCN (Zhang et al., 2012). Intense I.R spectral peak at 2060 cm^{-1} was attributed to stretching vibration modes of C≡N band and peak at 2790 cm^{-1} corresponded to C—H vibrations (Shanmugam et al., 2015). The broad bands appearing in range of 3100–3400 cm^{-1} positioned at 3107 and 3314 cm^{-1} were accredited to stretching vibration modes of N—H bond. A prominent peak at 518 cm^{-1} was assigned to stretching vibrations of Bi-O bonds in BiOBr (Liu et al., 2014). While peak at 712 cm^{-1} was attributed to asymmetrical stretching vibrations of Bi—O bond (Di et al., 2013).

3.1.2. FESEM and HRTEM

The morphological features of fabricated BiOBr/PSCN/Ag/AgCl were explored using FESEM and HRTEM study. SEM imageries of as-prepared photocatalyst were revealed in Fig. 3(a–f). Deposition of P and S dopants in the pores of GCN sheet resulted in characteristic lamellar sheet-like assembly of PSCN. Fig. 3(c) depicted flower like structure of BiOBr. Fig. 3(d) illustrated that AgCl exhibited different spherical as well as non-uniform structure. Fig. 3(e) shows clear agglomeration of BiOBr/Ag/AgCl nanoparticles. Fig. 3 (f) demonstrates successful deposition of BiOBr/Ag/AgCl nanoparticles onto PSCN sheet. EDX analysis was employed to calculate the elemental composition of the synthesized sample. Fig. S2 illustrated the existence of C, N, O, S, P, Ag, Cl, Bi and Br elements with weight percentage of 41.03%, 13.41%, 7.52%, 5.51%, 0.19%, 0.08%, 0.04%, 27.18% and 5.04% respectively confirmed the formation of BiOBr/PSCN/Ag/AgCl nanocomposite.

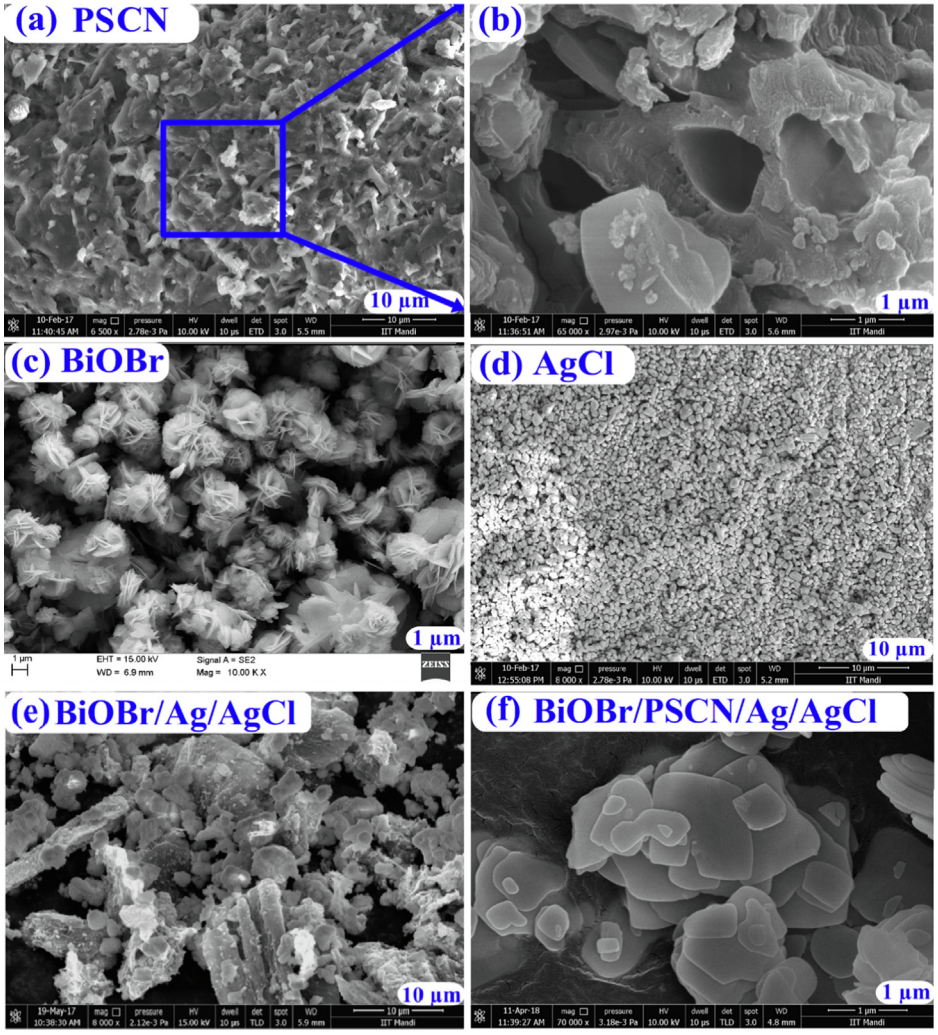

Fig. 3 FESEM images of (a) PSCN, (b) Exaggerated image of selected area, (c) BiOBr, (d) AgCl, (e) BiOBr/Ag/AgCl and (f) BiOBr/PSCN/Ag/AgCl.

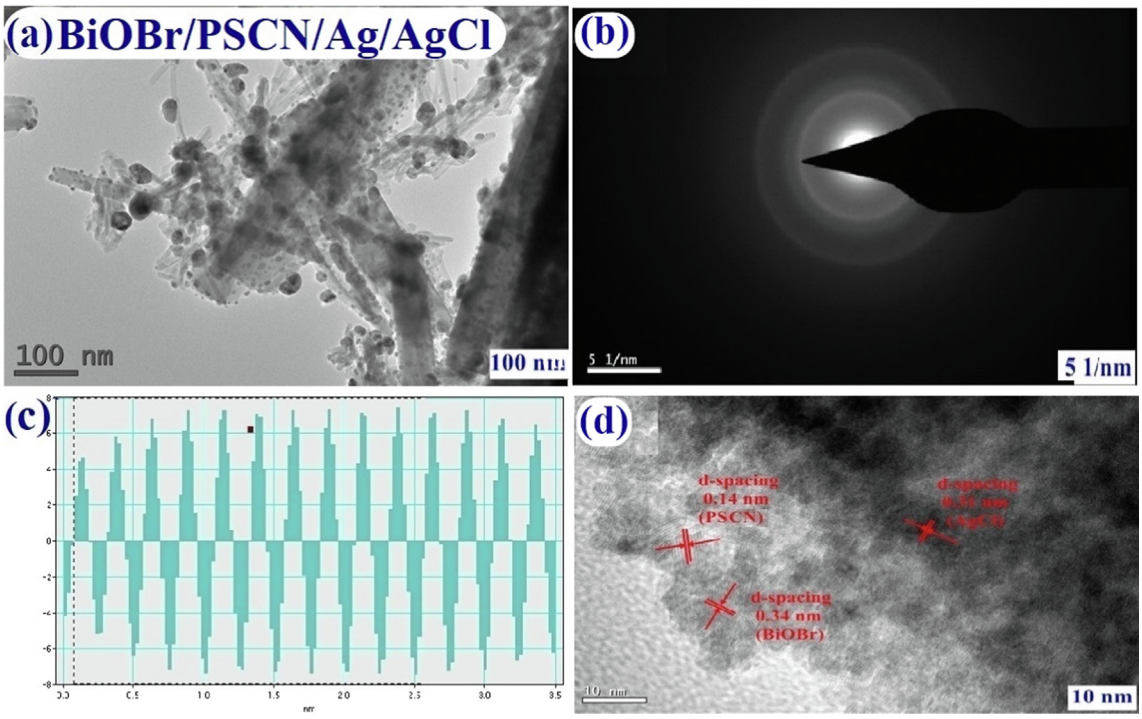

Fig. 4 HRTEM images of (a) BiOBr/PSCN/Ag/AgCl, (b) SAED pattern of as-prepared nanocomposite, (c) Demonstrates planar line profiles of BiOBr/PSCN/Ag/AgCl and (d) Exaggerated image of selected area.

Fig. 4(a–d) explicated TEM images of the synthesized nanocomposite. In Fig. 4(a) dispersion of AgCl and BiOBr nanoparticles on the surface of PSCN sheet was explored. Fig. 4(b) depicted SAED pattern of BiOBr/PSCN/Ag/AgCl photocatalyst. The interplanar spacing of BiOBr, PSCN and AgCl were found through planar spacing line profiles of BiOBr/PSCN/Ag/AgCl nanocomposite as shown in Fig. 4(c) which were found to be 0.14 nm, 0.31 nm and 0.34 nm (fringes with d spacing) for PSCN, AgCl and BiOBr, respectively illustrated in Fig. 4(d).

3.1.3. XPS analysis

Elemental composition and surface chemical state of BiOBr/PSCN/Ag/AgCl nanocomposite were recognized via XPS analysis and presence of phosphorus, sulfur, carbon, nitrogen, silver, chlorine, bismuth, oxygen and bromine were confirmed. (Fig. S3) displayed XPS Spectra of GCN, showing presence of Carbon and Nitrogen elements. For Carbon (C 1s) atom, binding energies were found at 284.1 eV and 288.0 eV which were ascribed to sp^2 C—C bond and C—O bonds in GCN, respectively (Fig. 3a). XPS spectrum of N 1s exhibited a sharp peak at 398.6 eV binding energy and was corresponded to pyridinic-N in GCN which was illustrated in Fig. 3b (Raizada et al., 2019a, Raizada et al., 2019c). Fig. 5(a) exposed peak at 133.4 was accredited to P-O-C and produced *via* substitution of carbon atom in PSCN framework (Wang et al., 2013a). In Fig. 5(b), S 2p spectrum two peaks (One sharp and one broad peak) at 162.4 and 167.2 eV were attributed to C—S bond and oxidized S (SO_x) respectively, specifying doping of S elements into GCN sheets *via* replacing nitrogen and carbon atom with sulphur (Ye et al., 2016). C 1s XPS spectrum was shown in Fig. 5(c) with peak positioned at 283.3 and 287.8 binding energies which were consigned with sp^2 C—C bond and C—O bonds in PSCN (Wang et al., 2013b). The sharp peak at 398.7 eV binding energy coincided with N 1s spectrum and resembled to pyridinic-N Fig. 5(d) (Guo et al., 2016). On the other hand, Fig. 5(e) displayed XPS spectrum of Ag. The peaks of Ag 3d spectrum revealed co-existence of two constituents in Ag $3d_{5/2}$ and Ag $3d_{3/2}$ signals, showing peaks at 367.5 and 368.2 eV for Ag $3d_{5/2}$ as well as 374.1 and 374.7 eV for Ag $3d_{3/2}$, respectively. The peaks at 367.5 and 374.1 were signified to Ag 3d peak inside AgCl (Ag^+), however the peaks at 368.2 and 374.7 eV were recognized to Ag^0 NPs peak, conferring to previous reports (Han et al., 2014; Wang et al., 2011). The 368.2 and 374.7 eV peaks displayed at lower binding energies established the existence of metallic AgNP in which pure silver cations (Ag^+) have been reduced to Ag^0 ion while left silver occurred in ionic state (Wang et al., 2014). The peaks located at 197.1 eV and 198.9 eV binding energy were allotted to characteristic doublets of Cl $2p_{3/2}$ and Cl $2p_{1/2}$, respectively in Fig. 5(f) (Chen et al., 2015). Fig. 5(g) showed two strong peaks at binding energies 158.3 eV and 164.3 eV which were related to Bi $4f_{5/2}$ and Bi $4f_{7/2}$ respectively and indicated presence of Bi element in BiOBr tri-valence state (Feng et al., 2011). Bi $4f_{5/2}$ and Bi $4f_{7/2}$ peaks exhibited slight shift in peaks compared to pure BiOBr due to minute contact in hybrid material but high resolution XPS spectrum of Br 3d Fig. 5(h) indicated broad band at 68.1 eV which was dispensed to Br $3d_{5/2}$ in BiOBr and BiOBr/Ag/AgCl (Tian et al., 2014). Intense peak displayed at 530.9 eV binding energy in Fig. 5(i) was associated to O 1 s of oxygen atom (Ji et al., 2015).

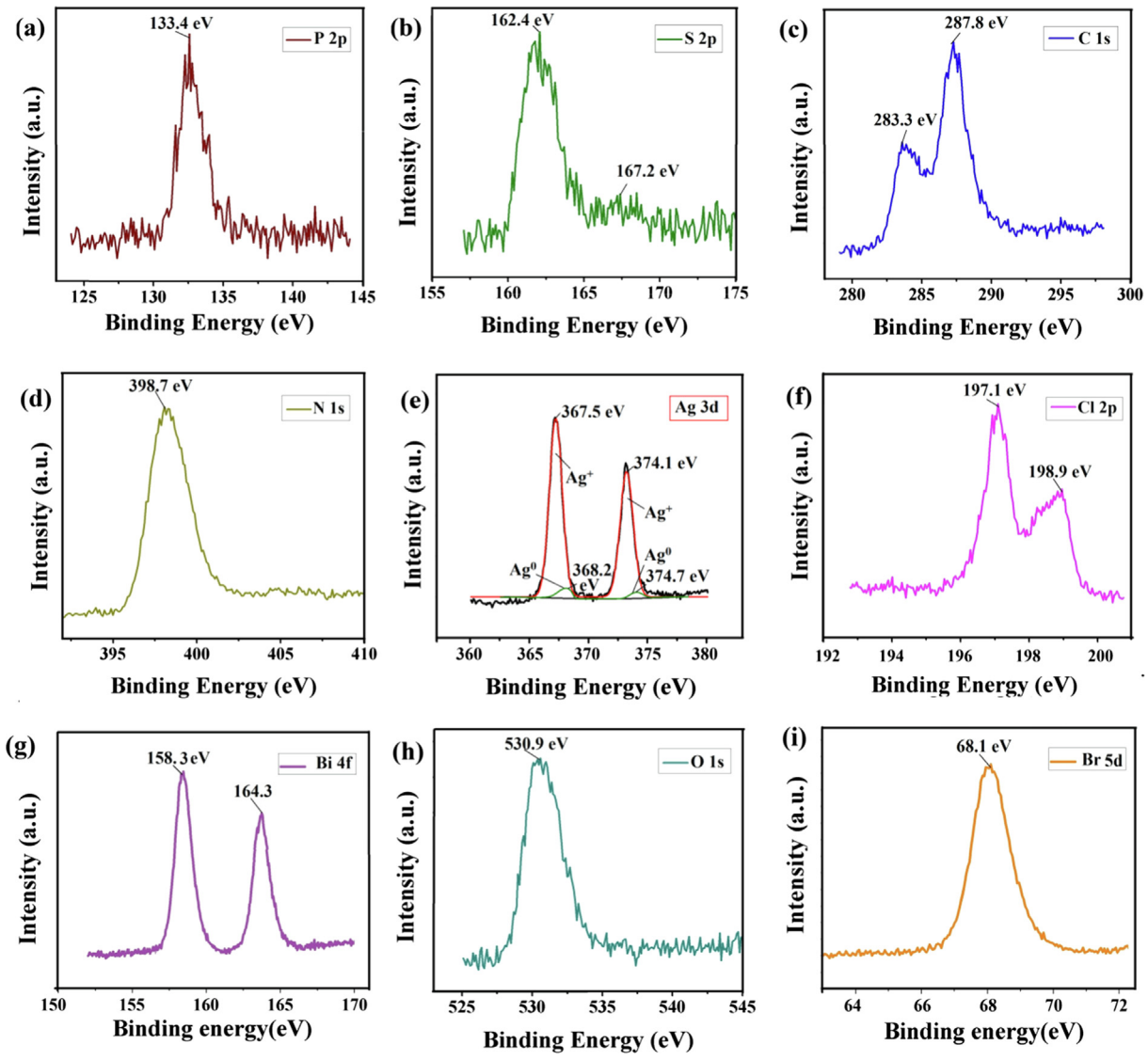

Fig. 5 XPS spectra of (a) P, (b) S, (c) C, (d) N, (e) Ag, (f) Cl, (g) Bi, (h) O and (i) Br in BiOBr/PSCN/Ag/AgCl heterojunction.

3.1.4. UV–visible, band gap and photoluminescence analysis

The UV–visible diffuse reflectance spectroscopy gave an idea about optical properties of BiOBr/PSCN/Ag/AgCl photocatalyst. Fig. 6(a) explicated the UV–vis absorption spectra of PSCN, BiOBr, AgCl, BiOBr/Ag/AgCl and BiOBr/PSCN/Ag/AgCl nanocomposite. Moreover, PSCN, AgCl and BiOBr exhibited fundamental absorption edge at 475 nm, 380 nm and 425 nm respectively. The incorporation of P and S dopants into porous GCN nanosheet enhanced visible light absorption thus producing photoinduced EHP (Wang et al., 2013a,b; Zheng et al., 2013). Extensively band gap of as synthesized nanocomposite was calculated in accordance with formula as follows (Singh et al., 2013; Sharma et al., 2019):

$$E_g = \frac{1240}{\lambda} \quad (2)$$

where λ is maximum absorption of fabricated photocatalysts. The optical band gap of PSCN, AgCl and BiOBr was reported to be 2.6 eV, 3.25 eV and 2.91 eV respectively which was consistent with previously reported work (Raizada et al., 2019a–d; Ye et al., 2014; Singh et al.,2018). From previous literature, it was investigated that addition of P and S co-dopants on GCN lattice caused reduction in band gap (Dong et al., 2014; Elham et al., 2016). The band gap energy of synthesized photocatalyst can be determined using Tauc's plots, as shown in Fig. 6(b).

The photoluminescence (PL) spectra predicted the charge separation in photoinduced reactions. The PL spectra of PSCN, BiOBr, AgCl, BiOBr/Ag/AgCl and BiOBr/PSCN/Ag/AgCl was shown in Fig. 6(c). The emission peak of PSCN was positioned at 455 nm. The fasten separation of photocarriers was due to inferior intensity of PSCN (Bourlinos et al., 2012). The PL emission peak of BiOBr/PSCN/Ag/AgCl heterojunction displayed decreased intensity as compared to pristine PSCN and BiOBr/Ag/AgCl binary heterojunction. Therefore, this decrease in intensity resulted in supressed recombination rate of photoinduced charge carriers.

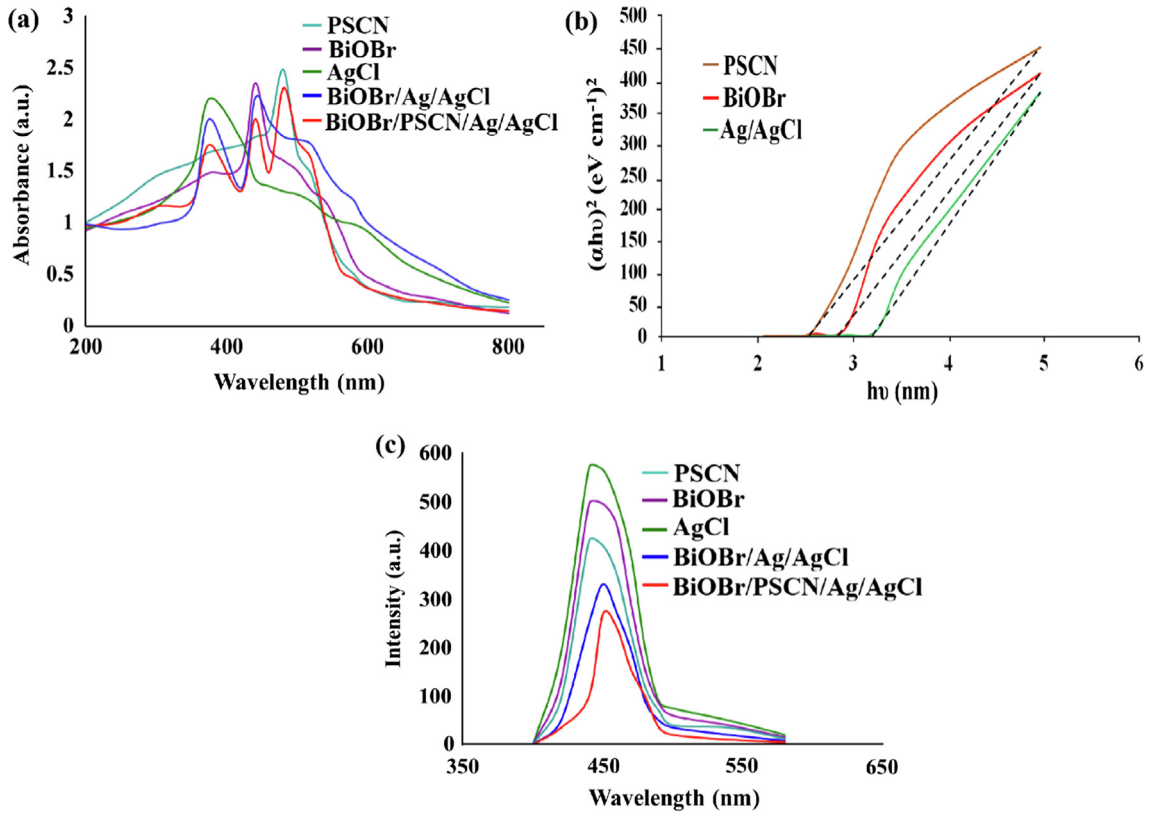

Fig. 6 (a) UV–visible analysis of PSCN, BiOBr/Ag/AgCl and BiOBr/PSCN/Ag/AgCl, (b) Tauc's plot of PSCN, BiOBr/Ag/AgCl and BiOBr/PSCN/Ag/AgCl and (c) PL spectra of PSCN, BiOBr/Ag/AgCl and BiOBr/PSCN/Ag/AgCl heterojunction.

3.2. Photocatalytic activity of BiOBr/PSCN/Ag/AgCl

3.2.1. Photocatalytic degradation of phenol by BiOBr/PSCN/Ag/AgCl nanocomposite

The photocatalytic activities of fabricated photocatalysts were measured by comparing photocatalytic degradation of phenol under halogen light. As it can be observed in Fig. 7(a–d), Ag/AgCl, BiOBr, PSCN and GCN exhibited low photocatalytic degradation efficiency, only 46%, 48%, 50% and 43% of phenol degradation in 60 min. However, BiOBr/Ag/AgCl, PSCN/Ag/AgCl, BiOBr/PSCN and BiOBr/PSCN/Ag/AgCl photocatalysts had 72%, 81%, 90% and 98% of phenol degradation in 60 min, respectively. In case of unitary photocatalysts, rapid recombination rate of photoinduced EHP retarded photodegradation of phenol. In BiOBr/Ag/AgCl, PSCN/Ag/AgCl, BiOBr/PSCN and BiOBr/PSCN/Ag/AgCl photoinduced EHP were effectively separated with excellent photooxidation ability for phenol degradation. Moreover, absence of photocatalyst had no effect on degradation of phenol, it confirmed the stability of phenol under solar light. The photodegradation ability of as-synthesized BiOBr/PSCN/Ag/AgCl nanocomposites was evaluated by examining the photodegradation of phenol under irradiation of visible light. Langmuir-Hinshelwood model explored the kinetics of degradation process and the following equations (Eqs. (3)–(5)) were employed for the study of photocatalytic performance for phenol degradation (Priya et al., 2016a; Singh et al., 2014; Dutta et al., 2019).

$$-\frac{dC}{dt} = kt \tag{3}$$

where C is the concentration of phenol at time t and k is rate constant. On integrating the above Eq. (3) between limits (0, C_0) and (t, C) we get,

$$-ln\left(\frac{c_t}{c_0}\right) = kt \tag{4}$$

$$ln\left(\frac{c_0}{c_t}\right) = kt \tag{5}$$

$\ln(C_0/Ct)$ *versus* time (t) plots were plotted for degradation of phenol (Raizada et al., 2019d). The linearity of $-\ln(C/C_0)$ *versus* time (t) plot signified pseudo first order kinetics during phenol degradation. The rate constants, 0.089, 0.082, 0.08, 0.07, 0.052, 0.050, 0.062 and 0.050 min^{-1} were calculated for phenol degradation using BiOBr/PSCN/Ag/AgCl (R^2, 0.98), BiOBr/PSCN (R^2, 0.95), PSCN/Ag/AgCl (R^2, 0.94), BiOBr/Ag/AgCl (R^2, 0.96), Ag/AgCl (R^2, 0.95), BiOBr (R^2, 0.97), PSCN (R^2, 0.96) and GCN (R^2, 0.96) photocatalyst, respectively (Table 1). The photodegradation experiment indicated higher photocatalytic activity for phenol degradation.

The degradation experiment was also performed in dark reaction conditions to evaluate the adsorption capacity of as prepared photocatalysts. The adsorption capacity followed the trend: BiOBr/PSCN/Ag/AgCl (34%) ≈ BiOBr/PSCN (33%) ≈ PSCN/Ag/AgCl (32%) ≈ PSCN (32%) ≈ GCN

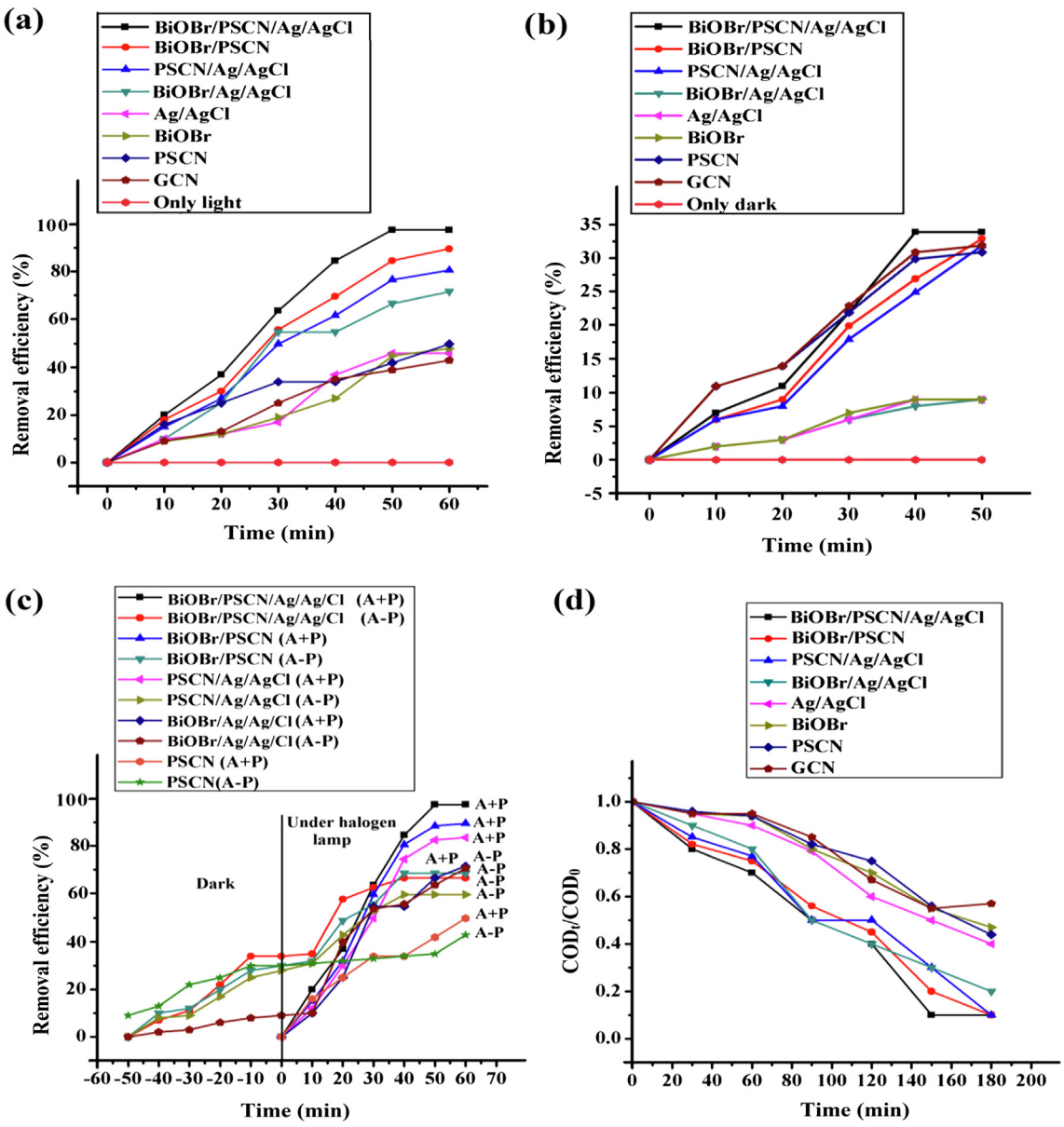

Fig. 7 (a) Photocatalytic degradation of phenol, (b) adsorptional removal of phenol, (c) time profile for removal of phenol under three reaction conditions and (d) COD removal. Reaction conditions: [phenol] = 1×10^{-4} mol dm^{-3}; [photocatalyst] = 50 mg/100 mL; initial reaction pH = 4.0 and Light intensity = 750 lx.

(31%) > BiOBr/Ag/AgCl (10%) ≈ Ag/AgCl (9%) ≈ BiOBr (9%). The adsorption results clearly indicated significant absorption capacity of PSCN and GCN for during phenol removal. While BiOBr/Ag/AgCl, Ag/AgCl and BiOBr did not have any significant adoption ability. Due to its extremely ordered tri-s-triazine (C_6N_7) units, graphitic carbon nitride can stack *viz* hydrophobic effect and π–π interaction. g-C_3N_4 can absorb organic/inorganic pollutants through conjugated π region, making g-C_3N_4 an effective adsorbent for water remediations (Raizada et al., 2019a–d).

The photocatalytic degradation reaction was significantly influenced by adsorption of aqueous phase toxins onto photocatalyst's surface. In order to check the effect of adsorption on photocatalysis of phenol, the photocatalytic process was subjected to two different reaction conditions: (i) simultaneous adsorption and photocatalysis (A + P) and (ii) adsorption followed by photocatalysis (A−P). It is clear that in case of BiOBr/PSCN/Ag/AgCl, BiOBr/PSCN, PSCN/Ag/AgCl and PSCN, A + P processes are more efficient than A-P process for photocatalytic degradation of phenol. During A-P process, extreme adsorption of phenol onto photocatalysts surface blocked visible light reaching to photoactive volume. So, overall photoactivity was reduced (Shandilya et al., 2019). However, during A + P, phenol molecules were concurrently degraded by photocatalysts under halogen lamp. Due to poor adsorption ability of BiOBr/Ag/AgCl, both A-P and A + P process had same photocatalytic ability for phenol degradation. It can be concluded that BiOBr/PSCN/Ag/AgCl A + P

Table 1 Rate constant the photodegradation of phenol. Reaction conditions: [Phenol] = 1.0×10^{-4} mol dm^{-3}; [catalyst] = 50 mg/100 mL; Initial reaction pH = 4.0; Time = 60 min. and Solar light intensity = 750 lx.

Photocatalyst	Rate constant (k) min^{-1}	R^2	% efficiency
BiOBr/PSCN/Ag/AgCl	0.089	0.98	98
BiOBr/Ag/AgCl	0.07	0.96	72
BiOBr/PSCN	0.082	0.95	33
PSCN/Ag/AgCl	0.08	0.94	32
Ag/AgCl	0.052	0.95	46
BiOBr	0.050	0.97	48
PSCN	0.062	0.96	50
GCN	0.050	0.96	43

was the most efficient of phenol degradation and further studies were under taken with A + P process.

3.2.2. Photo-mineralization of phenol

In order to explore the mineralization mechanism, COD and CO_2 estimation were performed during degradation process and results are given in Fig. 8(a–d). About 99% of COD was eliminated, employing BiOBr/PSCN/Ag/AgCl nanophotocatalyst during mineralization of phenol in 180 h. While during same reaction time, 80%, 60%, 53%, 54%, and 43% of COD removal was attainted using BiOBr/Ag/AgCl, Ag/AgCl, BiOBr, PSCN and GCN photocatalyst, respectively. The higher mineralization ability of BiOBr/PSCN/Ag/AgCl photocatalyst as higher as compared to bare PSCN, AgCl and BiOBr photocatalysts. CO_2 evolution during photodegradation process was due to phenol mineralization into nontoxic CO_2 and H_2O illustrated in Fig. S3. Moreover, High performance liquid chromatography (HPLC) analysis of degradation phenolic solution was performed to ascertain degradation process. Decreased peak intensity at retention time of 5 min was observed. During degradation process, a bunch of new peaks emerged between retention time 2–3 min followed by disappearance. It indicated the formation of degradation products during mineralization process. Furthermore, gas chromatography-mass spectrometry (GC–MS) study was performed using JEOL GCMATE II GC–MS equipped with C18 column (150 mm × 2 mm; injection volume 20 µL). The LC-MS analysis was performed for phenol sample after 60 min of photocatalysis under visible light. The different peaks were recorded at m/z ratios of 125 (phenol superoxide radical), 108 (hydroquinone/resorcinol/catechol and benzoquinone), 116 (maleic acid), 90 (oxalic acid), 93 (phenoxide ion) and 46 (formic acid) (Shandilya et al., 2018). The obtained peaks were also reported by Andre and co-workers during phenol degradation (Andrade et al., 2006). So, COD analysis along with analysis of reaction intermediates confirmed the mineralization of phenol into CO_2 and H_2O.

3.2.3. Mechanistic view of dual Z-scheme photocatalysis in BiOBr/PSCN/Ag/AgCl

The photocatalytic degradation process mainly involves reactive oxidative species like hydroxyl radicals ($OH^{\bullet}$), electrons

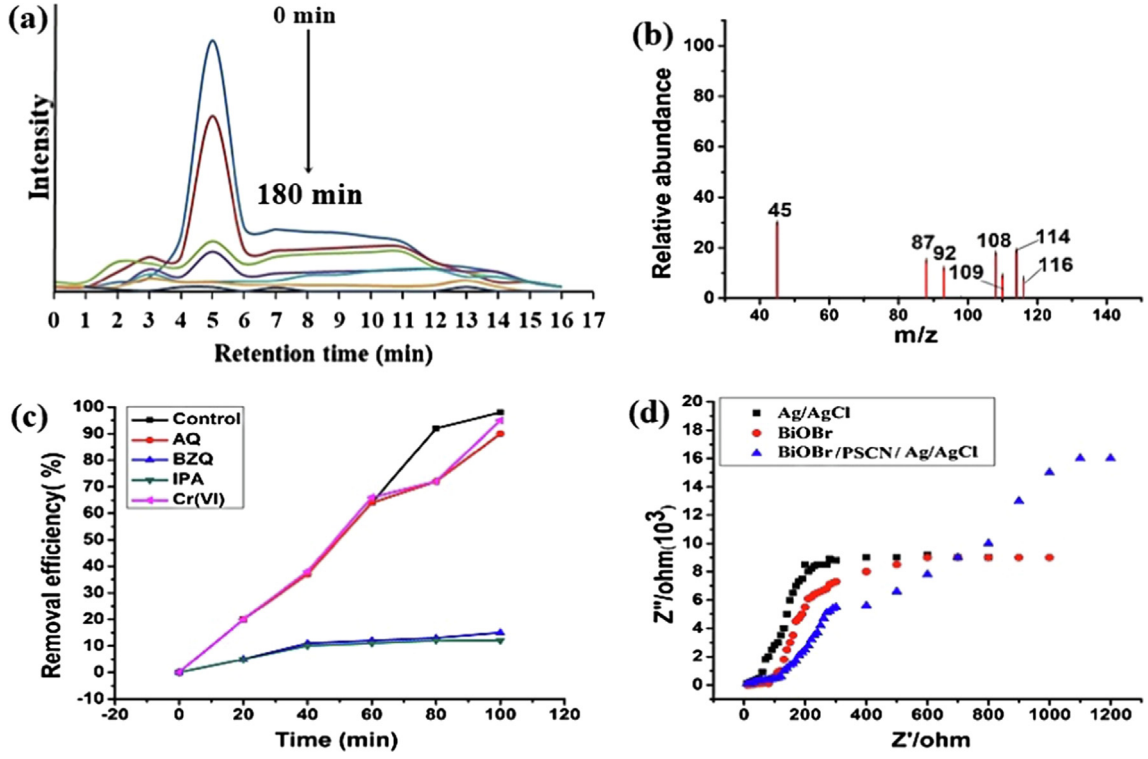

Fig. 8 (a) HPLC, (b)LC-MS analysis during mineralization of phenol, (c) Scavenging effects on photocatalytic degradation of phenol and (d) Electrochemical impedance spectroscopy (EIS) of BiOBr, Ag/AgCl and BiOBr/PSCN/Ag/AgCl nanocomposite. Reaction conditions: [phenol] = 1×10^{-4} mol dm^{-3}; scavenger] = 1×10^{-4} mol dm^{-3}; [photocatalyst] = 50 mg/100 mL; initial reaction pH = 4.0 and Light intensity = 750 lx.

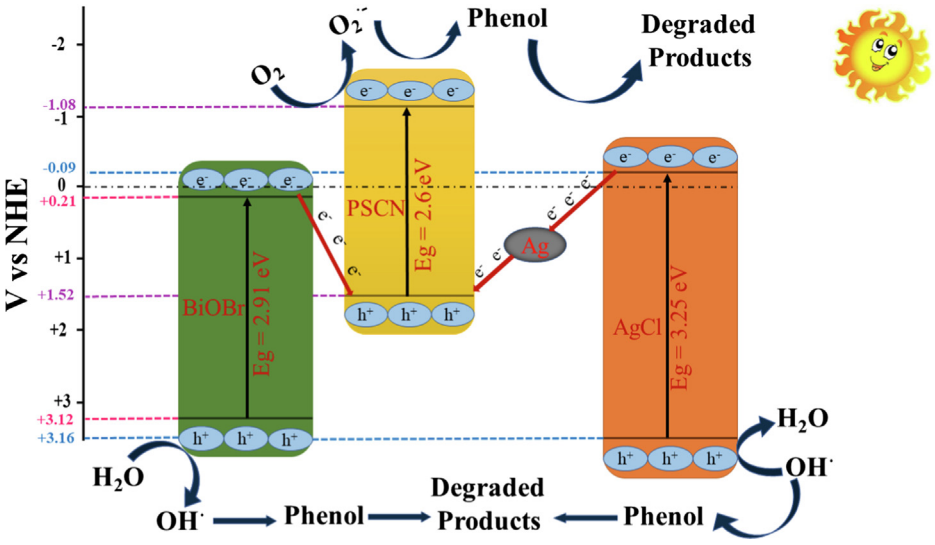

Fig. 9 Mechanistic view of BiOBr/PSCN/Ag/AgCl heterojunction for photocatalytic degradation of phenol.

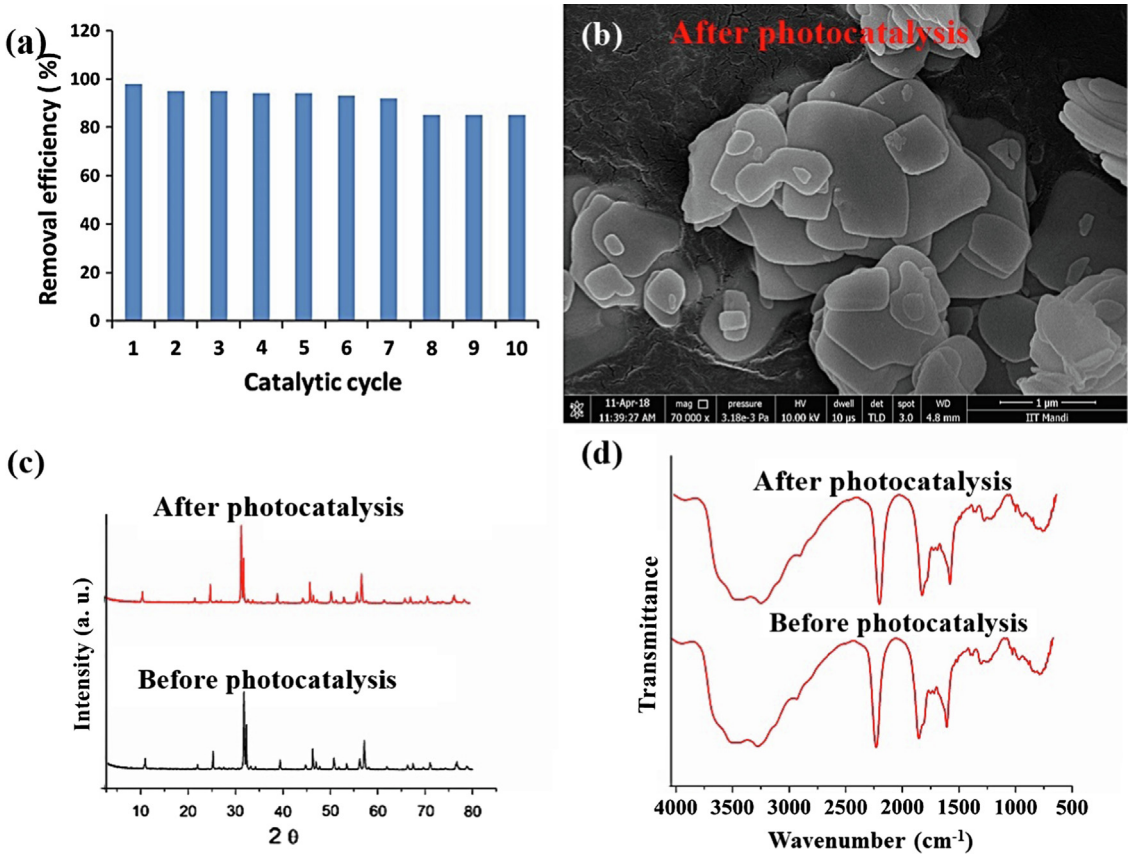

Fig. 10 (a) Recycle efficacy of BiOBr/PSCN/Ag/AgCl, (b), (c) and (d) SEM, XRD and FTIR analysis of photocatalyst after seven consecutive cycles. Reaction conditions: [phenol] = 1×10^{-4} mol dm^{-3}; [photocatalyst] = 50 mg/100 mL; initial reaction pH = 4.0 and Light intensity = 750 lx.

(e^-_{CB}), holes (h^+_{VB}), and superoxide radicals ($O_2^{\cdot-}$). In this work, Cr(VI) ion, ammonium oxalate (AO), isopropyl alcohol (IPA), and benzoquinone (BZQ) chosen as trapping agents for e^-_{CB}, h^+_{VB}, $OH^{\cdot}$ and $O_2^{\cdot-}$ radicals (Pare et al., 2008). During scavenging experiment for BiOBr/PSCN/Ag/AgCl photocatalyst, phenol degradation was reduced to 10% and 13% (MG dye) by adding IPA and BZQ to the reaction solution under solar light. On the other hand, addition of scavengers AO and Cr (VI) did not cause any noteworthy decrease in phenol degradation under halogen lamp. From scavenging experiments, it can be

summarized that $OH^{\cdot}$ and $O_2^{\cdot-}$ mainly contributed towards oxidative degradation of phenol. While, e^-_{CB} and h^+_{VB} did not contribute towards phenol mineralization.

The hydroxyl radicals ($OH^{\cdot}$), superoxide radicals ($O_2^{\cdot-}$), photogenerated holes (h^+_{CB}) and electrons (e^-_{VB}) are considered as reactive species during photodegradation of aqueous phase toxins (Raizada et al., 2019a–d). The VB and CB energy levels of the designed photocatalyst were calculated using following equation (Eq. (6), (7)):

$$E_{VB=}\chi - E^e + 0.5E_g \quad (6)$$

$$E_{CB=}E_{VB-}E_g \quad (7)$$

where χ denotes electronegativity of photocatalyst, E^e denotes energy of free electron at hydrogen scale (4.5 eV) and E_g is the photocatalyst bandgap. Under exposure to visible light, photo-illuminated charge carriers were produced on PSCN, AgCl and BiOBr. The VB and CB potentials of PSCN were estimated at −1.08 V and +1.52 V, respectively (Raizada et al., 2019a–d; Raizada et al., 2020). The CB potential of PSCN (−1.08 V) is more negative than the $O_2^{\cdot-}$ potential (−0.33 eV), therefore O_2 reacted with the photogenerated electrons in CB of PSCN to form $O_2^{\cdot-}$. Due to inferior VB potential of photoinduced holes (h^+) as compared to E_0 ($OH^{\cdot}$, H^+/H_2O = 2.72 V) they were unable to produce hydroxyl radicals ($OH^{\cdot}$). Therefore, under visible light irradiation $O_2^{\cdot-}$ were main reactive species for photodegradation of phenol (Jiang et al., 2012). Upon irradiation of visible light AgCl due to its wide band gap cannot be excited (Hou et al., 2013). AgCl possesses VB and CB potentials at +3.16 V and −0.09 V, respectively (Ye et al., 2014). The migration of charge carriers from CB of BiOBr and AgCl to VB of PSCN fulfilled the requirements of Z-scheme photocatalytic system (Jiang et al., 2018). Moreover, photoinduced electrons from CB of AgCl (-0.09 V) migrated to VB of PSCN (+1.52 V) *viz* Ag that acted as an electron transporter as illustrated in Fig. 9. Ag acted as electron mediator, moreover it improves the electron transfer capability of photocarriers. There was accumulation of holes in VB of BiOBr and AgCl. Due to the positive CB potential of BiOBr (+0.21 V) photoinduced electrons in CB of BiOBr do not react with O_2 to generate $O_2^{\cdot-}$, while radicals were generated as they react with H^+ and O_2 through following equations:

$$O_2 + 2e^- + 2H^+ \rightarrow H_2O_2 \quad (8)$$

$$H_2O_2 + 2e^- \rightarrow OH^{\cdot} + OH^- \quad (9)$$

The $OH^{\cdot}$ radicals produced in VB of BiOBr and AgCl were responsible for photodegradation of phenol into CO_2 and H_2O. Moreover, enhanced separation of photoinduced charge carriers in BiOBr/PSCN/Ag/AgCl was tested using electrochemical impedance spectroscopy (EIS) analysis. Fig. 8(d) illustrated EIS spectra of Ag/AgCl, BiOBr and BiOBr/PSCN/Ag/AgCl photocatalysts. The impedance arc size followed the trend: Ag/AgCl, BiOBr and BiOBr/PSCN/Ag/AgCl ≫ BiOBr ≈ Ag/AgCl. The highest arc size of BiOBr/PSCN/Ag/AgCl confirmed highest rate of separation of photogenerated charge carriers. The EIS spectra investigation was well supported by photoluminescence study of prepared photocatalysts. From above discussion, we concluded that transfer of photogenerated charge carriers from CB of both Ag/AgCl and BiOBr into VB of PSCN occurred *via* dual Z-scheme mechanism. Spatial separation of photoinduced EHP in BiOBr/PSCN/Ag/AgCl caused photodegradation of phenol into CO_2 and H_2O.

3.2.4. Recyclability and stability of BiOBr/PSCN/Ag/AgCl

Reusability and stability of photocatalyst is significant factor for real time utilization of photocatalyst. In present work, BiOBr/PSCN/Ag/AgCl photocatalyst was separated from reaction solution through centrifugation process and used for next photodegradation experiment. The photodegradation efficiency of photocatalyst was reduced to 90% from 98% after seven consecutive cycles as illustrated in Fig. 10. Moreover, FESEM, XRD and FTIR analysis of BiOBr/PSCN/Ag/AgCl did not show any significant modification in morphology and chemical composition (Raizada et al., 2020). It confirmed the stability of *BiOBr/PSCN/Ag/AgCl* for repeated cycles involving degradation of phenol and could be applied for real wastewater treatment.

4. Conclusion

In precedent work, a novel Z-scheme based BiOBr/PSCN/Ag/AgCl nanocomposite with enhanced photocatalytic activities were fabricated *via* hydrothermal process, moreover PSCN was synthesized by calcination method for waste water remediation. Incorporation of P and S co-dopants on surface of GCN lead to band gap lowering and extended absorption of solar light. Various techniques such as FESEM, HRTEM, XPS, XRD, EDX, FTIR, UV-DRS and PL analysis validated formation of BiOBr/PSCN/Ag/AgCl nanophotocatalyst. FESEM and HRTEM studies confirmed deposition of BiOBr/Ag/AgCl onto PSCN. While formation of BiOBr/PSCN/Ag/AgCl nanocomposite was confirmed by XPS, FTIR and EDX analysis. The as prepared BiOBr/PSCN/Ag/AgCl photocatalyst followed pseudo-first order kinetics for photodegradation of phenol. About 99% of COD was eliminated in 180 h during photodegradation process of phenol. The synthesized ternary BiOBr/PSCN/Ag/AgCl heterojunction revealed improved photocatalytic activities than bare BiOBr, PSCN and AgCl due to spatial charge separation followed by Z-scheme mechanism. Ag acted as an electron transporter among BiOBr, PSCN and AgCl which resulted in substantial decrease in recombination rate of photogenerated EHP. Degradation efficiency of prepared photocatalyst was reduced from 98% to 90% after seven consecutive cycles. Proposed mechanism explicated that $OH^{\cdot}$ and $O_2^{\cdot-}$ radicals were the reactive species responsible for mineralization of phenol. No considerable decrease was recorded for photocatalytic activity of BiOBr/PSCN/Ag/AgCl nanocomposite for successive 10 cycles.

Appendix A. Supplementary material

Supplementary data to this article can be found online at https://doi.org/10.1016/j.arabjc.2019.10.001.

References

Andrade, L.S., Laurindo, E.A., Oliveira, R.V.D., Rocha-Filho, R.C., Cass, Q.B., 2006. Development of a HPLC method to follow the degradation of phenol by electrochemical or photoelectrochemical treatment. J. Braz. Chem. Soc. 17, 369–373.

APHA, 1985. Standard Methods for Examination of Water and Wastewater, 6th ed., American PublicHealth Association, American Water Works Association, Water Environment Federation New York, pp. 535–543.

Banerjee, S., Dionysiou, D.D., Pillai, S.C., 2015. Self-cleaning applications of TiO_2 by photoinduced hydrophilicity and photocatalysis. Appl. Catal. B: Environ. 176, 396–428.

Bourlinos, A.B., Bakandritsos, A., Liaros, N., Couris, S., Safarova, K., Otyepka, M., Zboril, R., 2012. Water dispersible functionalized graphene fluoride with significant nonlinear optical response. Chem. Phys. Lett. 543, 101–105.

Chai, B., Yan, J., Wang, C., Ren, Z., Zhu, Y., 2017. Enhanced visible light photocatalytic degradation of Rhodamine B over phosphorus doped graphitic carbon nitride. Appl. Surf. Sci. 391, 376–383.

Chen, F., An, W., Liu, L., Liang, Y., Cui, W., 2017. Highly efficient removal of bisphenol A by a three-dimensional graphene hydrogel-AgBr@rGO exhibiting adsorption/photocatalysis synergy. Appl. Catal. B: Environ. 217, 65–80.

Chen, Y., Fang, J., Lu, S., Wu, Y., Chen, D., Huang, L., Fang, Z., 2015. Fabrication, characterization and photocatalytic properties of Ag/AgI/BiOI heteronanostructures supported on rectorite via a cation-exchange method Mater. Res. Bull. 64, 97–105.

Di, J., Xia, J., Yin, S., Xu, H., He, M., Li, H., Xu, L., Jiang, Y., 2013. A g-C_3N_4/BiOBr visible-light-driven composite: synthesis via a reactable ionic liquid and improved photocatalytic activity. RSC Adv. 3, 19624–19631.

Dong, L., Zhang, X., You, T., 2014. Electrochemical performance of electrospun free-standing nitrogen-doped carbon nanofibers and their application for glucose biosensing. ACS Appl. Mater. Interf. 6, 6275–6280.

Dutta, V., Singh, P., Shandilya, P., Sharma, S., Raizada, P., Saini, A. K., Gupta, V.K., Hosseini-Bandegharaei, A., Agarwal, S., Rahmani-Sani, A., 2019. Review on advances in photocatalytic water disinfection utilizing graphene and graphene derivatives-based nanocomposites. J. Environ. Chem. Eng. 7, (3) 103132.

Elham, A., Setayesh, S.R., Gholami, M.R., 2016. Synthesis of the visible-light-driven $Ag_3VO_4/Ag_3PO_4/Ag$ photocatalysts with enhanced photocatalytic activity. RSC Adv. 6, 14909–14915.

Feng, Y., Li, L., Li, J., Wang, J., Liu, L., 2011. Synthesis of mesoporous BiOBr 3D microspheres and their photodecomposition for toluene. J. Hazard. Mater. 192, 538–544.

Guo, J.F., Ma, B., Yin, A., Fan, K., Dai, W.L., 2012. Highly stable and efficient Ag/AgCl@ TiO_2 photocatalyst: preparation, characterization, and application in the treatment of aqueous hazardous pollutants. J. Hazard. Mater. 211–212, 77–82.

Guo, S., Deng, Z., Li, M., Jiang, B., Tian, C., Pan, Q., Fu, H., 2016. Phosphorus-doped carbon nitride tubes with a layered micro-nanostructure for enhanced visible-light photocatalytic hydrogen evolution. Angew. Chem. Int. Ed. 55, 1830–1834.

Han, C., Ge, L., Chen, C., Li, Y., Zhao, Z., Xiao, X., Zhang, J., 2014. Site-selected synthesis of novel Ag@ AgCl nanoframes with efficient visible light induced photocatalytic activity. J. Mat. Chem. 2, 12594–12600.

Hasija, V., Raizada, P., Sudhaik, A., Sharma, K., Kumar, A., Singh, P., Thakur, V.K., 2019. Recent advances in noble metal free doped graphitic carbon nitride based nanohybrids for photocatalysis of organic contaminants in water: A review. Appl. Mater. Today 15, 494–524.

Hou, J., Yang, C., Wang, Z., Ji, Q., Li, Y., Huang, G., Zhu, H., 2013. Three-dimensional Z-scheme AgCl/Ag/γ-TaON heterostructural hollow spheres for enhanced visible-light photocatalytic performance. Appl. Catal. B: Environ. 142, 579–589.

Hu, J., Zhang, P., An, W., Liu, L., Liang, Y., Cui, W., 2019. In-situ Fe-doped g-C_3N_4 heterogeneous catalyst via photocatalysis-Fenton reaction with enriched photocatalytic performance for removal of complex wastewater. Appl. Catal. B: Environ. 245, 130–142.

Ji, H., Jing, X., Xu, Y., Yan, J., Li, H., Li, Y., Huang, L., Zhang, Q., Xu, H., Li, H., 2015. Magnetic g-$C_3N_4/NiFe_2O_4$ hybrids with enhanced photocatalytic activity. RSC Adv. 5, 57960–57967.

Jiang, J., Li, H., Zhang, L.Z., 2012. New insight into day light photocatalysis of AgBr@Ag: Synergistic effect between semiconductor photocatalysis and plasmonic photo-catalysis. Chem. Eur. J. 18, 6360–6369.

Jiang, L., Yuan, X., Zeng, G., Chen, X., Wu, Z., Liang, J., Wang, H., 2017. Phosphorus-and sulphur-codoped g-C_3N_4: facile preparation, mechanism insight, and application as efficient photocatalyst for tetracycline and methyl orange degradation under visible light irradiation. ACS Sustain. Chem. Eng. 5, 5831–5841.

Jiang, M., Shi, Y., Huang, J., Wang, L., She, H., Tong, J., Wang, Q., 2018. Synthesis of Flowerlike g-C_3N_4/BiOBr with Enhanced Visible Light Photocatalytic Activity for Dye Degradation. Eur. J. Inorg. Chem. 17, 1834–1841.

Jiang, Z., Yang, F., Luo, N., Chu, B.T.T., Sun, D., Shi, H., Xiao, T., Edwards, P.P., 2008. Solvothermal synthesis of N-doped TiO_2 nanotubes for visible-light-responsive photocatalysis. Chem. Commun., 6372–6374

Jiang, Z., Yang, F., Yang, G., Kong, L., Jones, M.O., Xiao, T., Edwards, P.P., 2010. The hydrothermal synthesis of BiOBr flakes for visible-light-responsive photocatalytic degradation of methyl orange. J. Photochem. Photobiol. A 212, 8–13.

Jiao, Z., Zhang, J., Liu, Z., Ma, Z., 2019. Ag/AgCl/Ag_2MoO_4 composites for visible-light-driven photocatalysis. J. Photochem. Photobiol. A 371, 67–75.

Li, B., Shao, L., Zhang, B., Wang, R., Zhu, M., Gu, X., 2017. Understanding size-dependent properties of BiOCl nanosheets and exploring more catalysis. J. Colloid Interf. Sci. 505, 653–663.

Liu, Y., Bi, Y., Zhao, X., Zh, U., Huang, Y., 2014. Synthesis and photocatalytic property of BiOBr/palygorskite composites. Mater. Res. Bull. 49, 167–171.

Maiti, S.K., 2001. Handbook of Methods in Environmental Studies: Water and Wastewater Analysis. ABD Pub., Jaipur, India.

Natarajan, K., Bajaj, H.C., Tayade, R.J., 2016. Photocatalytic efficiency of bismuth oxyhalide (Br, Cl and I) nanoplates for RhB dye degradation under LED irradiation. J. Ind. Eng. Chem. 34, 146–156.

Pare, B., Singh, P., Jonnalgadda, S.B., 2008. Visible light induced heterogeneous advanced oxidation process to degrade pararosanilin dye in aqueous suspension of ZnO. Indian J. Chem. Sect. A 47, 830–835.

Pare, B., Singh, P., Jonnalgadda, S.B., 2009. Degradation and mineralization of Victoria blue B dye in a slurry photoreactor using advanced oxidation process. J. Sci. Ind. Res. 68, 724–729.

Priya, B., Raizada, P., Singh, N., Thakur, P., Singh, P., 2016a. Adsorptional photocatalytic mineralization of oxytetracycline and ampicillin antibiotics using Bi_2O_3/BiOCl supported on graphene sand composite and chitosan. J. Colloid Interface Sci. 479, 271–283.

Priya, B., Shandilya, P., Raizada, P., Thakur, P., Singh, N., Singh, P., 2016b. Photocatalytic mineralization and degradation kinetics of ampicillin and oxytetracycline antibiotics using graphene sand composite and chitosan supported BiOCl. J. Mol. Catal. A Chem. 423, 400–413.

Raizada, P., Priya, B., Thakur, P., Singh, P., 2016. Solar light induced photodegradation of oxytetracyline using Zr doped TiO_2/CaO based nanocomposite. Ind. J. Chem. 55A, 803–809.

Raizada, P., Sudhaik, A., Singh, P., Shandilya, P., Gupta, V.K., Bandegharaei, A.H., Agrawal, S., 2019a. Ag_3PO_4 modified phosphorus and sulphur co-doped graphitic carbon nitride as a direct Z-scheme photocatalyst for 2, 4-dimethyl phenol degradation. J. Photochem. Photobiol. A 374, 22–35.

Raizada, P., Sudhaik, A., Singh, P., Shandilya, P., Saini, A.K., Gupta, V.K., Hosseini-Bandegharaei, A., 2019b. Fabrication of Ag_3VO_4 decorated phosphorus and sulphur co-doped graphitic carbon

nitride as a high-dispersed photocatalyst for phenol mineralization and E. coli disinfection. Sep. Purif. Technol. 212, 887–900.

Raizada, P., Sudhaik, A., Singh, P., Hosseini-Bandegharaei, A., Thakur, P., 2019c. Converting type II AgBr/VO into ternary Z scheme photocatalyst via coupling with phosphorus doped g-C3N4 for enhanced photocatalytic activity. Sep. Purif. Technol. 12, 115692.

Raizada, P., Sudhaik, A., Singh, P., Shandilya, P., Thakur, P., Jung, H., 2020. Visible light assisted photodegradation of 2, 4-dinitrophenol using Ag_2CO_3 loaded phosphorus and sulphur co-doped graphitic carbon nitride nanosheets in simulated wastewater. Arab J. Chem 13, 3196–3209. https://doi.org/10.1016/j.arabjc.2018.10.004.

Raizada, P., Sudhaik, A., Singh, V.P., Gupta, V.K., Hosseini-Bandegharaei, A., Kumar, R., Singh, P., 2019d. Solar light assisted degradation of oxytetracycline from water using Bi_2O_3/Fe_3O_4 supported graphitic carbon nitride photocatalyst. Desalin Water Treat. 148, 338–350.

Shandilya, P., Mittal, D., Soni, M., Raizada, P., Lim, J.H., Jeong, D. Y., Singh, P., 2018. Islanding of $EuVO_4$ on high-dispersed fluorine doped few layered graphene sheets for efficient photocatalytic mineralization of phenolic compounds and bacterial disinfection. J. Taiwan Inst. Chem. E. 93, 528–542.

Shandilya, P., Mittal, D., Sudhaik, A., Soni, M., Raizada, P., Saini, A. K., Singh, P., 2019. $GdVO_4$ modified fluorine doped graphene nanosheets as dispersed photocatalyst for mitigation of phenolic compounds in aqueous environment and bacterial disinfection. Sep. Purif. Technol. 210, 804–816.

Sharma, K., Dutta, V., Sharma, S., Raizada, P., Hosseini-Bandegharaei, A., Thakur, P., Singh, P., 2019. Recent advances in enhanced photocatalytic activity of bismuth oxyhalides for efficient photocatalysis of organic pollutants in water: A review. J. Ind. Eng. Chem. 78, 1–20.

Shanmugam, M., Alsalme, A., Alghamdi, A., Jayavel, R., 2015. Enhanced photocatalytic performance of the graphene-V_2O_5 nanocomposite in the degradation of methylene blue dye under direct sunlight. ACS Appl. Mater. Interfaces 7, 14905–14911.

Singh, P., Raizada, P., Kumari, S., Kumar, A., Pathania, D., Thakur, P., 2014. Solar-Fenton removal of malachite green with novel Fe^0-activated carbon nanocomposites. Appl. Catal. A General. 476, 9–18.

Singh, P., Raizada, P., Pathania, D., Kumar, A., Thakur, P., 2013. Preparation of BSA-$ZnWO_4$ nanocomposites with enhanced adsorptional photocatalytic activity for methylene blue degradation. Int. J. Photoenergy 2013, 1–7.

Singh, P., Raizada, P., Sudhaik, A., Shandilya, P., Thakur, P., Agarwal, S., Gupta, V.K., 2018. Enhanced photocatalytic activity and stability of AgBr/BiOBr/graphene heterojunction for phenol degradation under visible light In Press J. Saudi. Chem. Soc. https://doi.org/10.1016/j.jscs.2018.10.005.

Sudhaik, A., Raizada, P., Shandilya, P., Jeong, D.Y., Lim, J.H., Singh, P., 2018a. Review on fabrication of graphitic carbon nitride based efficient nanocomposites for photodegradation of aqueous phase organic pollutants. J. Ind. Eng. Chem. 67, 28–51.

Sudhaik, A., Raizada, P., Shandilya, P., Singh, P., 2018b. Magnetically recoverable graphitic carbon nitride and $NiFe_2O_4$ based magnetic photocatalyst for degradation of oxytetracycline antibiotic in simulated wastewater under solar light. J. Environ. Chem. Eng. 6, 3874–3883.

Tang, Y., Subramaniam, V.P., Lau, T.H., Lai, Y., Gong, D., Kanhere, P.D., Cheng, Y.H., Chen, Z., Dong, Z., 2011. In situ formation of large-scale Ag/AgCl nanoparticles on layered titanate honey comb by gas phase reaction for visible light degradation of phenol solution. Appl. Catal. B: Environ. 106, 577–585.

Tian, H., Fan, Y., Zhao, Y., Liu, L., 2014. Elimination of ibuprofen and its relative photo-induced toxicity by mesoporous BiOBr under simulated solar light irradiation. RSC Adv. 4, 13061–13070.

Wang, L., Sun, Y., Zhou, P., Wan, P., Zhang, X., Qiu, J., 2013a. P/N co-doped microporous carbons from H_3PO_4-doped polyaniline by in situ activation for supercapacitors. Carbon 59, 537–546.

Wang, P., Huang, B., Zhang, X., Qin, X., Dai, Y., Wang, Z., Lou, Z., 2011. Highly Efficient Visible Light Plasmonic Photocatalysts Ag@ Ag (Cl, Br) and Ag@ AgCl-AgI. Chem Cat Chem. 3, 360–364.

Wang, R., Qiu, G., Xiao, Y., Tao, X., Peng, W., Li, B., 2019. Optimal construction of $WO_3{\cdot}H_2O$/Pd/CdS ternary Z-scheme photocatalyst with remarkably enhanced performance for oxidative coupling of benzylamines. J. Catal. 374, 378–390.

Wang, S.M., Li, D.L., Sun, C., Yang, S.G., Guan, Y., He, H., 2014. Synthesis and characterization of g-C_3N_4/Ag_3VO_4 composites with significantly enhanced visible-light photocatalytic activity for triphenyl methane dye degradation. Appl. Catal. B: Environ. 144, 885–892.

Wang, W.D., Huang, F.Q., Lin, X.P., Yang, J.H., 2008. Visible-light responsive photocatalysts BiOBr (1–x) BiOI. Catal. Commun. 9, 8–12.

Wang, X.J., Yan, W.Y., Li, F.T., Xue, Y.B., Liu, R.H., Hao, Y.J., 2013b. In situ microwave-assisted synthesis of porous N-TiO_2/g-C_3N_4 heterojunctions with enhanced visible-light photocatalytic properties. Ind. Eng. Chem. Res. 52, 17140–17150.

Wang, Y., Zhou, J., Hao, X., Wang, Y., Zou, Z., 2018. Fabricating direct Z-scheme PTCDA/g-C_3N_4 photocatalyst based on interfacial strong interaction for efficient photooxidation of benzylamine. Appl. Surf. Sci. 456, 861–870.

Xia, J., Di, J., Yin, S., Li, H., Xu, H., Xu, L., He, M., 2014. Solvothermal synthesis and enhanced visible-light photocatalytic decontamination of bisphenol A (BPA) by g-C_3N_4/BiOBr heterojunctions. Mat. Sci. Semicon. Proc. 24, 96–103.

Xiao, Y., He, Z., Wang, R., Tao, X., Li, B., 2019a. Synthesis of WO_3 nanofibers decorated with BiOCl nanosheets for photocatalytic degradation of organic pollutants under visible light. Colloid Surf. A: Physiochem. Eng. Asp. 580, 123752.

Xiao, Y., Tao, X., Qiu, G., Dai, Z., Gao, P., Li, B., 2019b. Optimal synthesis of a direct Z-scheme photocatalyst with ultrathin $W_{18}O_{49}$ nanowires on g-C_3N_4 nanosheets for solar-driven oxidation reactions. J. Colloid Interf. Sci. 550, 99–109.

Yanhui, A., Wang, K., Wang, P., Wang, C., Hou, J., 2016. Synthesis of novel 2D–2D p-n heterojunction BiOBr/$La_2Ti_2O_7$ composite photocatalyst with enhanced photocatalytic performance under both UV and visible light irradiation. Appl. Catal. B: Environ. 194, 157–168.

Ye, L., Su, Y., Jin, X., Xie, H., Zhang, C., 2014. Recent advances in BiOX (X= Cl, Br and I) photocatalysts: synthesis, modification, facet effects and mechanisms. Environ. Sci. Nano 1, 90–112.

Ye, L., Wang, D., Chen, S., 2016. Fabrication and Enhanced Photoelectrochemical Performance of MoS_2/S-Doped g-C_3N_4 Heterojunction Film. ACS Appl. Mater. Interfaces 8, 5280–5289.

Zhang, G., Zhang, J., Zhang, M., Wang, X., 2012. Polycondensation of thiourea into carbon nitride semiconductors as visible light photocatalysts. J. Mater. Chem. 22, 8083–8091.

Zhang, J.T., Liu, X., Suo, X.Y., Li, P.J., Liu, B.K., Shi, H.Z., 2017. Facile synthesis of Ag/AgCl/TiO_2 plasmonic photocatalyst with efficiently antibacterial activity. Mater. Lett. 198, 164–167.

Zhang, X., Zhang, L., Xie, T., Wang, D., 2009. Low-temperature synthesis and high visible-light-induced photocatalytic activity of BiOI/TiO_2 heterostructures. J. Phys. Chem. C. 113, 7371–7378.

Zhang, Y., Cui, W., An, W., Liu, L., Liang, Y., Zhu, Y., 2018. Combination of photoelectrocatalysis and adsorption for removal of bisphenol A over TiO_2-graphene hydrogel with 3D network structure. Appl. Catal. B: Environ. 221, 36–46.

Zhao, Z., Sun, Y., Dong, F., 2015. Graphitic carbon nitride-based nanocomposites: a review. Nanoscale 7, 15–37.

Zheng, L., Nie, H., Yang, Z., Zhang, J., Jin, Z., Lu, Y., Xiao, Z., Huang, S., 2013. Sulfur–nitrogen co-doped three-dimensional carbon foams with hierarchical pore structures as efficient metal-

free electrocatalysts for oxygen reduction reactions. Nanoscale 5, 3283–3288.

Zhou, T., Xu, Y., Xu, H., Wang, H., Da, Z., Huang, S., Ji, H., Li, H., 2014. In situ oxidation synthesis of visible-light-driven plasmonic photocatalyst Ag/AgCl/g-C_3N_4 and its activity. Ceram. Int. 40, 9293–9301.

Zhou, Y., Zhang, L., Liu, J., Fan, X., Wang, B., Wang, M., Shi, J., 2015. Brand new P-doped g-C_3N_4: enhanced photocatalytic activity for H_2 evolution and Rhodamine B degradation under visible light. J. Mater. Chem. A 3, 3862–3867.